**PAPER • OPEN ACCESS**

# Photothermal superhydrophobic copper nanowire assemblies: fabrication and deicing/defrosting applications

View the article online for updates and enhancements.

# Photothermal superhydrophobic copper nanowire assemblies: fabrication and deicing/defrosting applications

**Siyan Yang**[1,2,4]**, Qixun Li**[1,4]**, Bingang Du**[1]**, Yushan Ying**[1]**, Yijun Zeng**[2]**, Yuankai Jin**[2]**, Xuezhi Qin**[2]**, Shouwei Gao**[2]**, Steven Wang**[2]**, Zuankai Wang**[3]**, Rongfu Wen**[1] **and Xuehu Ma**[1,*] [ORCID]

[1] State Key Laboratory of Fine Chemicals & Frontier Science Center for Smart Materials, School of Chemical Engineering, Dalian University of Technology, Dalian 116024, People's Republic of China
[2] Department of Mechanical Engineering, City University of Hong Kong, Hong Kong 999077, People's Republic of China
[3] Department of Mechanical Engineering, The Hong Kong Polytechnic University, Hong Kong 999077, People's Republic of China

E-mail: xuehuma@dlut.edu.cn

CrossMark

## Abstract

Ice and frost buildup continuously pose significant challenges to multiple fields. As a promising de-icing/defrosting alternative, designing photothermal coatings that leverage on the abundant sunlight source on the earth to facilitate ice/frost melting has attracted tremendous attention recently. However, previous designs suffered from either localized surface heating owing to the limited thermal conductivity or unsatisfied meltwater removal rate due to strong water/substrate interaction. Herein, we developed a facile approach to fabricate surfaces that combine photothermal, heat-conducting, and superhydrophobic properties into one to achieve efficient de-icing and defrosting. Featuring copper nanowire assemblies, such surfaces were fabricated via the simple template-assisted electrodeposition method, allowing us to tune the nanowire assembly geometry by adjusting the template dimensions and electrodeposition time. The highly ordered copper nanowire assemblies facilitated efficient sunlight absorption and lateral heat spreading, resulting in a fast overall temperature rise to enable the thawing of ice and frost. Further promoted by the excellent water repellency of the surface, the thawed ice and frost could be spontaneously and promptly removed. In this way, the all-in-one design enabled highly enhanced de-icing and defrosting performance compared to other nanostructured surfaces merely with superhydrophobicity, photothermal effect, or the combination of both. In particular, the defrosting efficiency could approach $\sim$100%, which was the highest compared to previous studies. Overall, our approach demonstrates a promising path toward designing highly effective artificial deicing/defrosting surfaces.

Supplementary material for this article is available online

Keywords:  nanowire, photothermal, superhydrophobic, de-icing, defrosting

# 1. Introduction

Ice and frost accumulation on material surfaces continuously pose significant and ongoing challenges across various fields, ranging from cryogenic freezing of nanoscale cells to flight of macroscale aircrafts. When covered by ice or frost in humid and subzero environments, these systems may suffer from cell disorganization, light obstruction, heat transfer deterioration, and equipment failure, to name a few [1–3]. Traditional de-icing/defrosting solutions mainly rely on mechanical, thermal, and chemical approaches, such as mechanical abrasion, ultrasonic vibration, electrical heating, or deicing fluids, yet, all of which are either energy-intensive, labor-intensive, or environmentally unfriendly [4–6]. Moreover, some of these active approaches required direct contact with the material surface, which easily damaged fragile surface coatings, thus compromising their original functions [7].

To achieve energy-saving and eco-friendly deicing/defrosting without deteriorating the surface functions, most efforts have shifted towards passive approaches via surface modifications, such as superhydrophobic surfaces [8, 9], slippery surfaces [10–12], phase-change/magnetic material-comprised surfaces [13, 14], low interfacial toughness coatings [15, 16]. Of special interest are superhydrophobic surfaces with weak liquid-solid interfacial interaction. This enabled easy shedding of deposited/coalesced water droplets, or self-removal of frost layers through peeling off or jumping off mechanisms [17–23]. Moreover, a superhydrophobic surface typically outperforms a surface with much higher water/substrate interaction (e.g. hydrophilic surface) regarding de-icing and defrosting, due to the water-repellency property [24–27]. Despite promising and effective, the previous attempts are normally unable to spontaneously remove the attached ice or frost under cold environments unless there is sufficient heat input to enable the melting of ice/frost [28, 29]. Recently, photothermal surfaces capable to be heated by sunlight, a green energy source abundant on the earth, have attracted significant attention [30–32]. It even seems more promising and effective to explore the fusion of photothermal and superhydrophobic properties in surface design, yet most surfaces suffer from localized and uneven heating due to the inferior thermal conductivity [33–36]. As a result, the surface area shaded by ice or frost still underwent a limited temperature increment, which compromised the de-icing/defrosting speed and efficiency. To this end, further assembling these surface properties with thermally conductive materials, especially metals [20, 37], holds great potential for de-icing and defrosting, which, yet, remains largely unexplored.

Here, we develop a facile fabrication approach to produce controllable copper nanowire assemblies that incorporate all three aforementioned properties, which enables superior deicing and defrosting performances. Our fabrication process involves the use of an anodic oxidation process to obtain anodic aluminum oxide (AAO) and a two-step electroplating process to create nanowires, assisted by AAO templates. The resulting copper nanowires can be self-assembled into highly controlled, ordered patterns. Among these patterns, we found that the upright morphology with small microgroove size (1–3 $\mu$m) demonstrated superior performance in de-icing and defrosting compared to other nanostructured surfaces that exclusively possessed superhydrophobicity, photothermal effect, or the combination of both. Specifically, our design was able to accelerate the melting of both frozen water and frost layers, resulting in 2–3 times shorter in overall defrosting durations than other three nanostructured surfaces and the highest defrosting efficiency ($\sim$100%) compared to previous works.

# 2. Design and fabrication of nanowire assemblies

The fabrication approach involves two main steps. First, AAO templates are fabricated via an anodic oxidation method (figure 1(a)). Briefly, the aluminate sheet after the annealing treatment and oxide layer removal was electropolished, followed by the anodization to obtain porous AAO templates with uniform nanochannels. Second, assisted by the AAO templates, we fabricated nanowire assemblies by the electrodeposition approach (figure 1(b), more details in Methods). These nanowire assemblies were modified with a low-surface-energy monolayer to endow them with superhydrophobicity. Our findings suggest that our copper nanowire assemblies are highly promising for photothermal de-icing and defrosting applications, due to their superior photothermal effect, high thermal conductivity, and superhydrophobicity, as depicted in figure 1(c). Specifically, the unique morphology of our copper nanowire assemblies allows for efficient longitudinal heat absorption, while the copper material facilitates fast lateral heat conduction. These properties enable the heat to be transported to the overall surface region, effectively melting either a frozen droplet or a frost layer. Further promoted by the infused water-repellency property, the surface allows for melted water to easily roll off with just a small tilt angle.

To achieve controllability in the morphology of nanowire assemblies necessitates the control in both geometrical dimensions of AAOs (such as the distance and diameter of pores) and the electroplating time. This is accomplished by controlling the applied voltage and solution composition, which enables us to obtain AAO sheets (figure 2(a)) with even arrangements of nanochannels on the surface (figure 2(b)). On one hand, the pore distance $L$ of AAO shows a linear relationship with voltage $U$, which follows $L = \sigma (40n + 195m)$, where $\sigma$ normally equals to 2.5 nm V$^{-1}$ [24, 38], and $n$ and $m$ are the volume fraction of oxalic acid and phosphoric acid. On the other hand, the pore diameter $D$ is tailored by adjusting the pore-widening time $t$ using 5 wt.% phosphoric acid at 30 °C. The use of oxalic acid results in smaller initial pore sizes, whereas the use of phosphoric acid leads to larger sizes (figure S1). As shown in figure 2(c), we observe linear relationships between the pore diameter $D$ and the pore-widening time $t$, given by $D = 3.1t + 25.3$ for oxalic acid or $D = 2.3t + 176$ for phosphoric acid. These linear relationships confirm the feasibility of precisely controlling the pore distance and pore size, which can serve as effective templates to fabricate nanowires using electroplating.
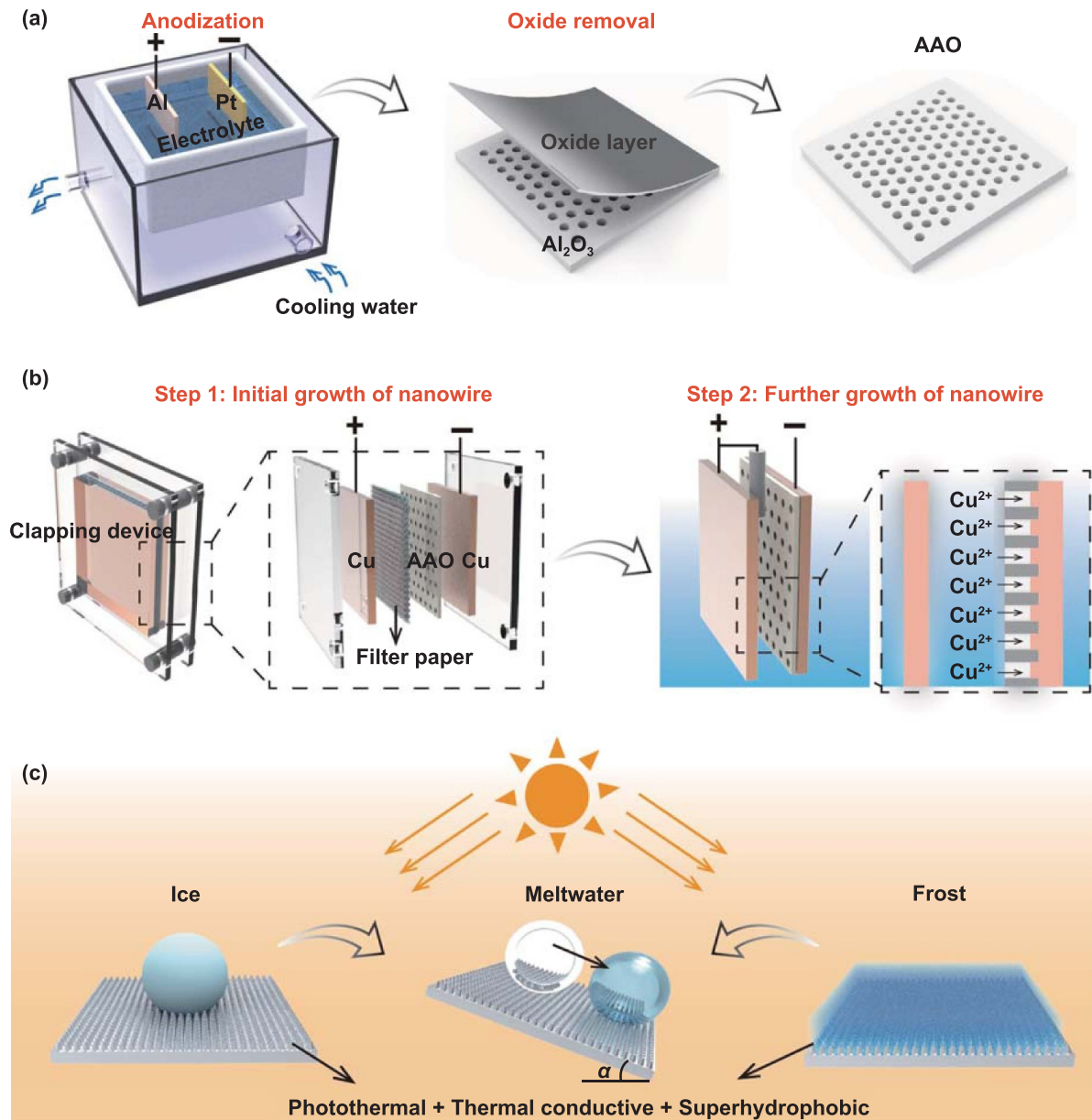
**Figure 1.** Fabrication and design of nanowire assemblies. (a) Schematic showing the fabrication of AAO, involving anodization and oxide layer removal steps. (b) Schematic of fabricating nanowire assemblies, involving the initial nanowire growth using a clapping device and the further nanowire growth inside a galvanic bath. (c) Owing to the combination of photothermal, thermal conductive, and superhydrophobic properties of the nanowire assemblies, both the frozen droplet and frost can melt quickly and roll off spontaneously from the tilted surface upon sunlight illumination.

Upon dissolving the AAO template, the resulting nanowires were free at one end. After a subsequent drying process, nanowires tended to bend laterally and cluster or even intertwine with each other due to the capillary force combined with the liquid/vapor menisci between the free ends of the soft nanowires [39]. Figure 2(d) illustrates the six orders of nanowire assembly morphologies, which become increasingly intertwined as the solid fraction $\varphi$ decreases. The solid fraction can be calculated by considering the hexagonal arrangement of the pores, using the equation $\varphi = \pi D^2/(2\sqrt{3}L^2)$. Furthermore, a longer electroplating time that brings taller nanowires can lead to similar conclusion (figure S2). Altogether, nanowires

that are long, thin or sufficiently spaced apart are more prone to deformation.

The deformation of nanowires can be ascribed to a decrease in bending stiffness or an increase in capillary attraction, a phenomenon in reminiscence of the clumping in wet hair [40] in human life, or tarsi of beetles [41] and spiders in nature [42]. We can construct a set of rough criteria for simple scaling analysis. The bending stiffness of a single released nanowire $B$ scales as $B \sim ED^4$, where $E$ is Young's modulus, $D$ is the diameter of nanowire. For nanowires within a solution that contact together, the bending force scales as $F_B \sim BL/H^3$, where $L$ and $H$ are distance and length of nanowires, respectively.
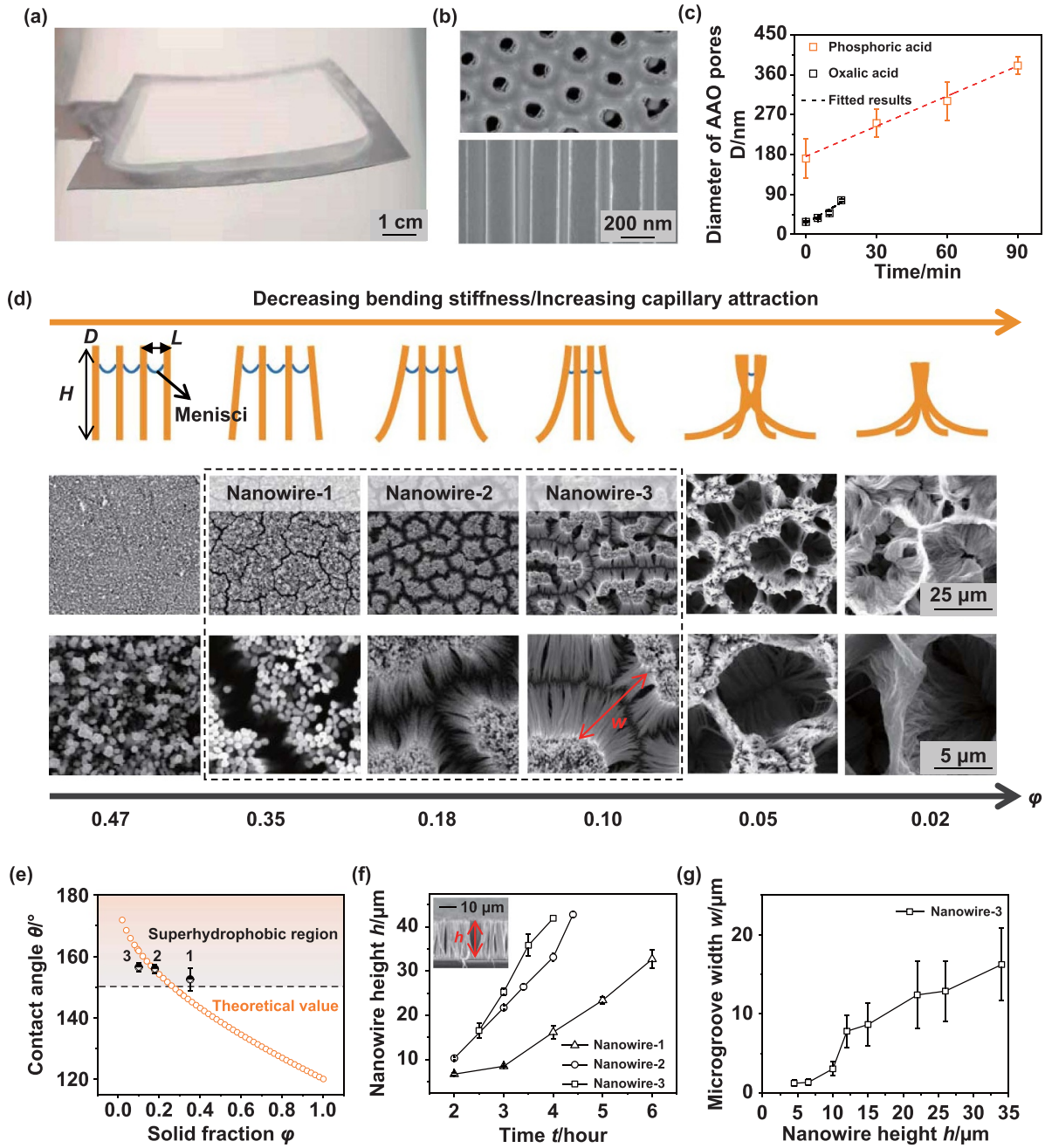
**Figure 2.** Control over the morphologies of nanowire assemblies. (a) Optical image showing the as-fabricated AAO sheet with a size of 8 cm × 8 cm × 50 $\mu$m. (b) The SEM images showing the uniform pores of the AAO sheet from a top view and side view. (c) The variation of pore diameter as a function of the pore widening time in oxalic acid or phosphoric acid. The black dashed line represents the fitted line. (d) Schematic diagrams and corresponding scanning electron microscopy (SEM) images showing the self-organized morphologies of nanowire assemblies after three hours of electroplating, from upright and separate to intertwined and twisted as a function of solid fraction $\varphi$. From left to right, the pictures respectively represent the orders of morphology from the first to the sixth. The black dashed circle represents the samples used in the photothermal experiments. (e) After the superhydrophobic treatment, the experimental contact angle $\theta$ of three chosen nanowire assemblies agrees with the theoretical value. (f) Height $h$ of nanowire assembly as a function of electroplating time $t$. (g) The variation of average microgroove width $w$ with the change of $h$.

The capillary attraction due to the menisci connecting the free ends can be expressed as $F_C \sim \gamma D$, where $\gamma$ is the liquid tension force [43]. When the bending force becomes comparable to the capillary force, a critical nanowire length exists, given by $H_C \sim (EL/\gamma)^{1/3}D$, above which the capillary force will maintain contact between the nanowire free ends. As the liquid continues to evaporate, competition arises between the adhesion force between nanowires and the bending force of the nanowires. Assume that the adhesion energy per unit area is $J$ [44], the adhesive force can be described as $F_A \sim JD$. Thus, it exists another characteristic length that scales as $H_A \sim (EL/J)^{1/3}D$. When $H_A > H > H_C$, nanowires will come into

contact with each other during the drying process, but they will eventually separate, resulting in an upright morphology similar to the first and second-order morphologies. When $H > H_A$ and $H > H_C$, nanowires tend to form clusters, like the third and fourth-order morphologies. When $H \gg H_A$, the enormous adhesive force relative to the bending force makes nanowires bend to a great extent and even twist with each other, just like the fifth and sixth-order morphologies [39]. Based on these analyses, we can obtain the desired nanowire morphologies by tuning the critical parameters mentioned above.

The morphology of nanowire assemblies results in distinct photothermal and superhydrophobic properties. To identify nanowire assemblies that simultaneously exhibit photothermal and superhydrophobic properties, we considered two criteria. First, the micro/nano structures necessitate high sunlight absorption and low light reflection capabilities. To evaluate this, we conducted reflectance measurements using a spectrophotometer instrument. The average solar reflectance $\rho_{avg}$ is defined as: $\rho_{avg} = \frac{\int_{0.3}^{2.5} I(\lambda) \cdot \rho(\lambda) d\lambda}{\int_{0.3}^{2.5} I(\lambda) d\lambda}$, where $\lambda$ is the wavelength of the incident light, $I(\lambda)$ is the normalized ASTM G173 Global solar intensity spectrum, and $\rho(\lambda)$ is the surface spectral reflectance [45, 46]. Reflectance measurements revealed that, among the six surfaces, there was a slight increase in sunlight reflection as the order increased, except for the first-order nanowire surface, as evidenced in figure S3. Second, the surfaces should possess a relatively small solid fraction to ensure a contact angle larger than 150°, according to $\cos\theta = \varphi(\cos\theta_Y + 1)^{-1}$, where $\theta_Y$ is the intrinsic contact angle [47].

Based on the analyses above, we rationally chose the second to fourth-order nanowire assemblies featuring nanowire bundles and microgrooves, namely Nanowire-1, Nanowire-2, and Nanowire-3. These nanowire assemblies showed excellent superhydrophobicity, with a contact angle larger than 150° (figure 2(e)) and a sliding angle less than 10°. Additionally, we were able to control the key morphology parameters of these three nanowire assemblies. Figure 2(f) illustrates that the height of the nanowire assemblies, denoted by $h$, exhibited a linear increase as a function of the electroplating time. Furthermore, the average width of the microgrooves, represented by $w$, was found to be closely correlated with the nanowire height $h$ (figure 2(g)).

## 3. Photothermal performance of nanowire surface

To gain a deeper understanding of the superior de-icing and defrosting performance of the selected nanowires, we compared their key properties to those of three other nanostructures commonly used in previous works, referred to as nanoparticle, nanograss, and commercial surfaces. Figure 3(a) displays the morphologies of these surfaces. Firstly, we observed that all surfaces exhibited superhydrophobicity, with a water contact angle larger than 150° and a sliding angle less than 10° (figure 3(b)). Next, we utilized an infrared camera to investigate the photothermal performance of the tested surfaces. To ensure accurate infrared imaging settings, we measured the

spectral emissivity of surfaces using a spectrometer, as exhibited in figure S4. Under one-sun illumination (1000 W m$^{-2}$) for 10 min, as exemplified by the Nanowire-1, its surface temperature could climb to around 30 °C from the initial −10 °C (figure 3(c)). Moreover, it delivered a distinctly faster temperature rise than other nanostructured surfaces within 60 s, as shown in figure S5. To explore the reason, we further compared the solar reflectance of all surfaces (figure 3(d)). The averaged reflectance of Nanowire-1, Nanowire-2, and Nanowire-3 was 3.5%, 3.8%, and 5.9%, a little higher than that of nanoparticle (1.5%) and nanograss surfaces (2.3%). Thus, the counterintuitive faster temperature rise on Nanowire-1 surface compared to other nanostructured surfaces may be attributed to its higher thermal conductivity. Among all samples, the thermal conductivity of nanowires made of copper is much higher than others made of carbon particles, cupric oxide, and silicone particles. The overall thermal conductivity $k'$ of these nanostructures can be expressed as $k' = k \cdot \varphi + k_{air} \cdot \varphi_{air}$. Here, $k$ is the thermal conductivity of the corresponding bulk materials, with copper, carbon, copper oxide, and epoxy resin in the magnitude of $\sim 10^2$, $\sim 10^{-2}$, $\sim 10$, and $10^{-1}$ W m$^{-1}$·K [48, 49], respectively. $k_{air}$ is the thermal conductivity of air (0.026 W m$^{-1}$·K). $\varphi$ is the solid fraction of nanostructured surfaces, which can be calculated by Cassie-Baxter equation [48, 50], $\cos\theta_a^{CB} = \varphi_e(\cos\theta_a + 1) - 1$, $\theta_a$ is the advancing water contact angle of the smooth hydrophobized surface, which is normally less than 120° but larger than 90°, and $\theta_a^{CB}$ is the advancing angle under Cassie state, which corresponded to a value larger than 150° (nanoparticle surface for 153°, nanograss surface for 155°, and commercial surface for 158°). After the careful calculation, we can deduce that the solid fractions of three nanostructured surfaces were less than 0.26. $\varphi_{air}$ is the fraction of the air within the surface structure and $\varphi_{air} = 1 - \varphi$, thus the contribution of the air in the overall thermal conductivity is negligible. Considering the solid fraction of nanowire surface was larger than 0.26, the overall thermal conductivity $k'$ of nanowire surface can be at least one order of magnitude higher than that of other nanostructured surfaces. Thus, the highest temperature rise of Nanowire surface resulted from a comprehensive contribution from both superior photothermal effect and the highest thermal conductivity.

As the precision of infrared imaging could be affected by environmental conditions, we further used thermal couples with high precision to confirm the photothermal performance at a cold ambient temperature of −10 °C (figure 3(e)). Considering the practical solar intensity under cloudy weather, or at afternoon or midday, we also studied the temperature variation under three sun illumination intensities, involving 0.5, 1, and 1.5 sun (figures 3(f)–(h)). Among all the tested surfaces, Nanowire-1 displayed the highest temperature rise under all sun illumination intensities. Notably, the difference in final temperature between Nanowire-1 and Nanograss surfaces could reach ∼10 °C under one-sun illumination. Based on these findings, we selected Nanowire-1 for de-icing and defrosting experiments and referred to it as Nanowire surface
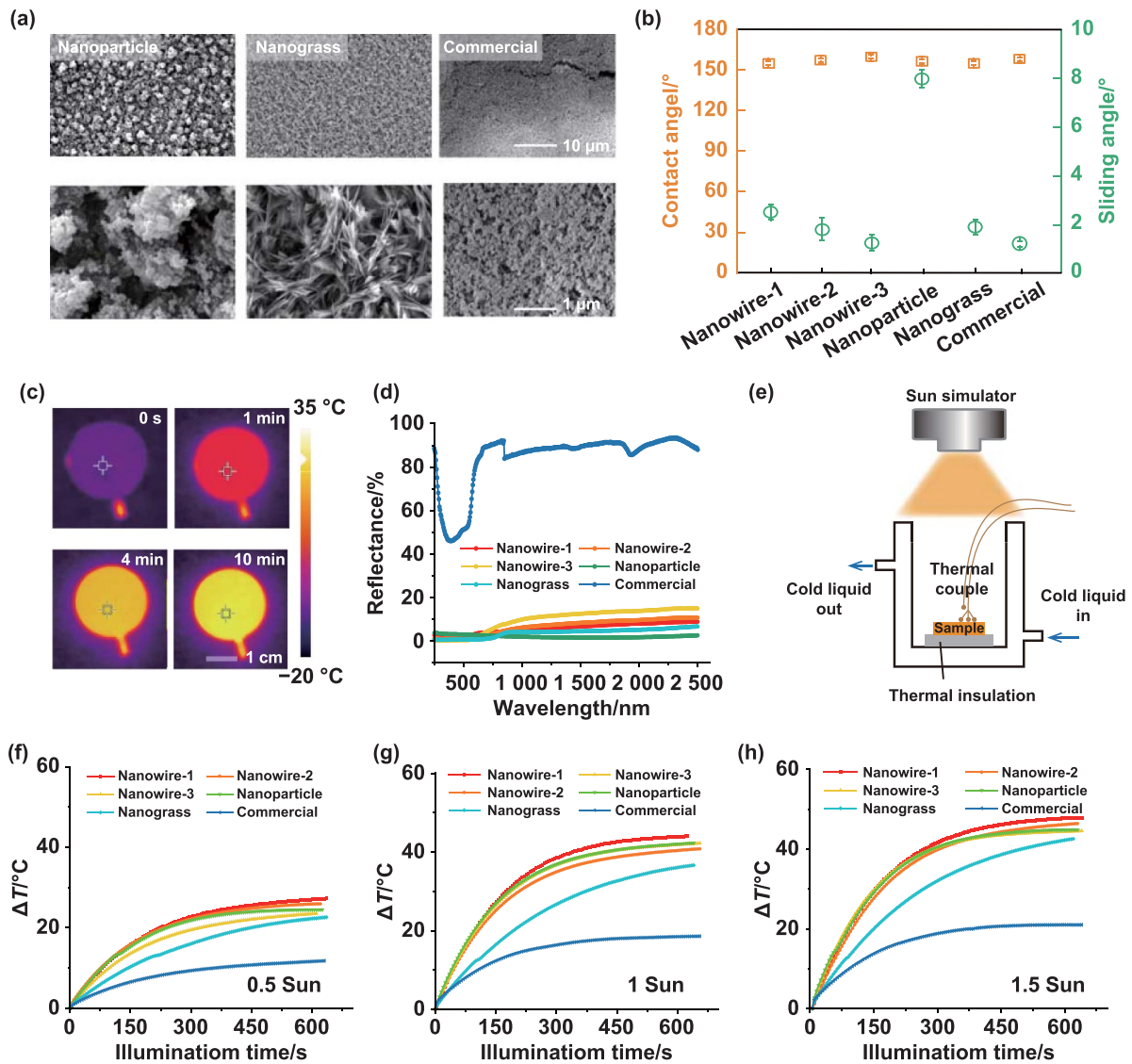
**Figure 3.** Characterization of photothermal properties. (a) The SEM images of three nanostructured surfaces. (b) Contact angle and sliding angle of tested samples. (c) Infrared camera images of Nanowire-1 surface under 1 sun. (d) Spectral reflectivity of different nanostructures from 0.3 to 2.5 $\mu$m. (e) Schematic of temperature measurement via thermal couples. (f)–(h) Increment of surface temperature measured by thermal couples under 0.5, 1, 1.5 sun at $T_s = -10\,°C$, RH $= 20 \pm 3\%$, $T_{air} = -10 \pm 1\,°C$.

in the following sections. Furthermore, based on our experimental data, we determined the local solar-thermal conversion efficiency $\eta_{solar\text{-}th}$ of the tested samples. Nanowire-1 surface exhibited similar $\eta_{solar\text{-}th}$ as that of nanoparticle and nanograss surface, all of which reached ~87% (more details in supplementary information). However, due to the difference in lateral thermal conductivity and structure-induced surface wettability, the final de-icing and defrosting performance can significantly vary, as discussed in the following sections.

## 4. Deicing and defrosting performances

After identifying the key properties of the tested samples, particularly the photothermal effect, we proceeded to study their de-icing and defrosting performances. Figure 4(a) schematic-

ally shows the advantage of nanowire surface in promoting ice melting. Upon sun illumination, nanowires functioned as a heat absorber as well as thermal spreader, resulting in fast and efficient heat transportation across the entire surface and promoting the melting of frozen droplet, as confirmed in figure S6. To quantitatively demonstrate this advantage, we compared the durations required to initiate and complete the melting of a frozen droplet at substrate temperatures of −15, −20, and −25 °C, as shown in figure 4(b). As expected, nanowire surface required the shortest time to initiate as well as complete the melting, due to its fastest temperature rise of the substrate underlying the droplet. In striking contrast, commercial surface was unable to heat the ice droplet, regardless of the substrate temperature (−15, −20, or −25 °C), due to its high sunlight reflectance, making the frozen droplet remain in a solid state.
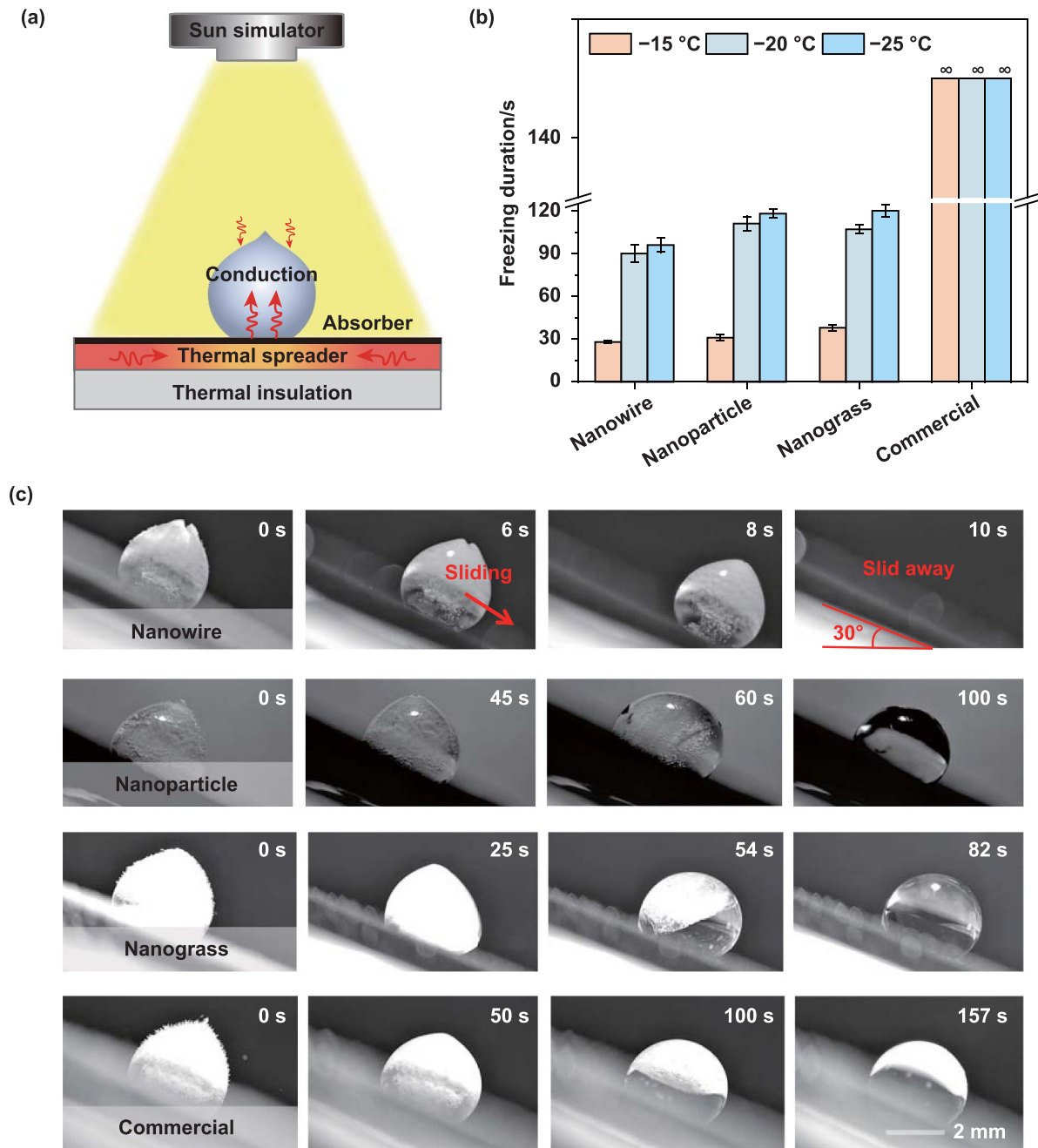
**Figure 4.** Photothermal de-icing performance. (a) Schematic of a frozen droplet on a horizontal nanowire surface exposed to sun illumination. The nanowires served as both a thermal absorber and thermal conductor, where heat can be fast transported to the entire surface and thus heating the frozen droplet. (b) Time required for initiating and completing the droplet melting on four horizontally placed surfaces after the droplet was frozen at −15 °C, −20 °C, and −25 °C. (c) Snapshots of droplet melting on four surfaces with a tilt angle after being frozen at −5 °C. Nanowire surface was the only one that launched the fast slide of the melting droplet.

We further investigated the de-icing behavior of the surfaces when given a slight tilt angle. Despite all surfaces undergoing hydrophobic treatment, resulting in a contact angle greater than 150°, and contact angle hysteresis less than 10°, only Nanowire surface enabled droplet sliding after melting. As shown in figure 4(c), on Nanowire surface with a tilt angle of 30°, the bottom of the frozen droplet, which primarily received heat, began to melt after 6 s under one-sun illumination. Upon melting, the interface between the droplet and substrate became a slippery water layer, allowing for quick

droplet sliding and shedding before complete melting. In contrast, the frozen droplet remained anchored and pinned on the other three surfaces even after complete melting (more details provided in movie S1).

The above distinction in de-icing performance lies in whether the surface textures can prevent droplet pinning. It should be noted that the deposited droplet on a cold surface inevitably undergoes droplet evaporation and subsequent vapor condensation [51]. The nanowires, with their dense and ordered structure and much larger height (>10 $\mu$m) than
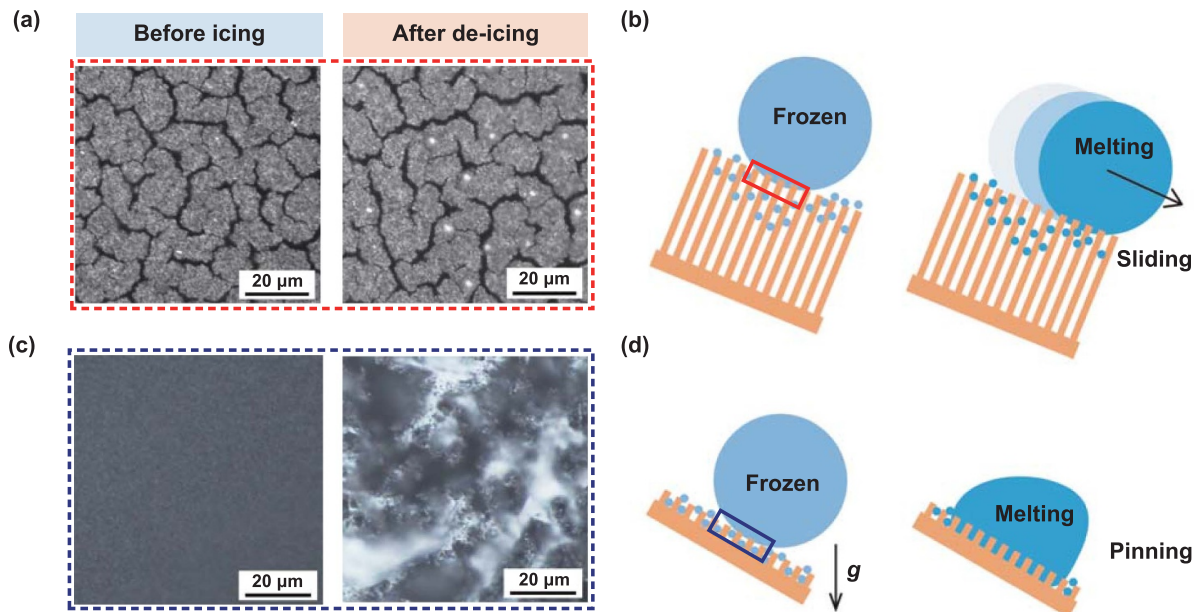
**Figure 5.** De-pinning effect on nanowire surface. (a) Optical images showing the morphology before icing and after de-icing of nanowire surface, where white circles represent condensed droplets. (b) Schematics of droplet rolling on nanowire surface after sun illumination. (c) Optical images showing the morphology before icing and after de-icing of the other three nanostructures. As exemplified by nanoparticle surface, a water film existed on the surface after de-icing. (d) Schematics of droplet pinning on three nanostructured surfaces after sun illumination.

other nanostructures ($<1$ $\mu$m), could effectively prevent water vapor from penetrating the underlying surface texture [52], as shown in figure 5(a), thereby inhibiting the formation of a liquid bridge between the substrate and the droplet. This finally endowed the melted droplet with a highly mobilized Cassie state to allow the easy rolling from the surface with superhydrophobicity, as depicted in figure 5(b). These results stood in highly contrast to those observed on the other three random and disordered nanostructures, on which the condensed water could form a liquid film in the Wenzel state to pin the water droplet, as exemplified by Nanoparticle surface in figure 5(c) (more details in figure S7), thus preventing the pinned droplet from shedding, as depicted in figure 5(d).

Apart from icing, frosting is another common scenario that necessitates consideration. We conducted a systematic investigation of the defrosting capabilities of nanowire surface under 0.5, 1, and 1.5 sun illuminations. After 1 h of frost accumulation at $T_s = -10$ °C and then exposed to one-sun illumination, nanowire surface was able to completely shed the melted frost, as shown in figure 6(a). Notably, it enabled the melting frost layer to roll up, merge, and completely self-shoot from the surface. In contrast, the other surfaces retained either a small or large amount of meltwater after the defrosting process (more details in movie S2). This discrepancy lies in the force competition during frost melting. The frost slurry typically consisted of ice on the top layer and water on the bottom layer due to the lower density of ice compared to water [53], making it kinetically unstable under the unbalanced interfacial tension forces between the ice/water and water/substrate, as shown in figure 6(b). On nanowire surface, the resultant force

is along the inward and upward direction due to the negligible water/substrate interfacial interaction, allowing the frost slurry to rapidly curl and shed off the surface as a whole. Conversely, the water/substrate interaction on other nanostructured surfaces was much stronger than that on nanowire surface, as explained in the de-icing part, preventing the frost slurry from self-curling and self-shedding from the surface. Consequently, the frost melted into sparsely distributed slurries retained on the surfaces.

To acquire a quantitative understanding in the defrosting efficiency, we measured the delay of frost melting and overall defrosting duration under different sun illuminations and frozen durations. As shown in figures 6(c) and (d), nanowire surface consistently showed the shortest delay in frost melting and the overall frost melting duration, regardless of the frozen duration. Notably, the difference in these two durations between the nanowire surface and the other three surfaces could be as much as 2 or 3-fold, demonstrating the advantage of nanowire surface in both rapid frost melting and shedding. Such advantage was also evident under different sun illuminations (figure S8). Moreover, we also considered the defrosting efficiency, defined as the ratio of frost removal, and compared it with previous studies that employed different strategies such as hydrophilic, hydrophobic, superhydrophobic, slippery surfaces, and surfaces exhibited both photothermal and superhydrophobic properties [28, 32, 54–60]. As shown in figure 6(e), while some of the surfaces used in previous studies exhibited a defrosting efficiency over 90%, nanowire surface demonstrated an impressively high defrosting efficiency approaching 100%, demonstrating the best defrosting efficiency among all the reported surfaces.
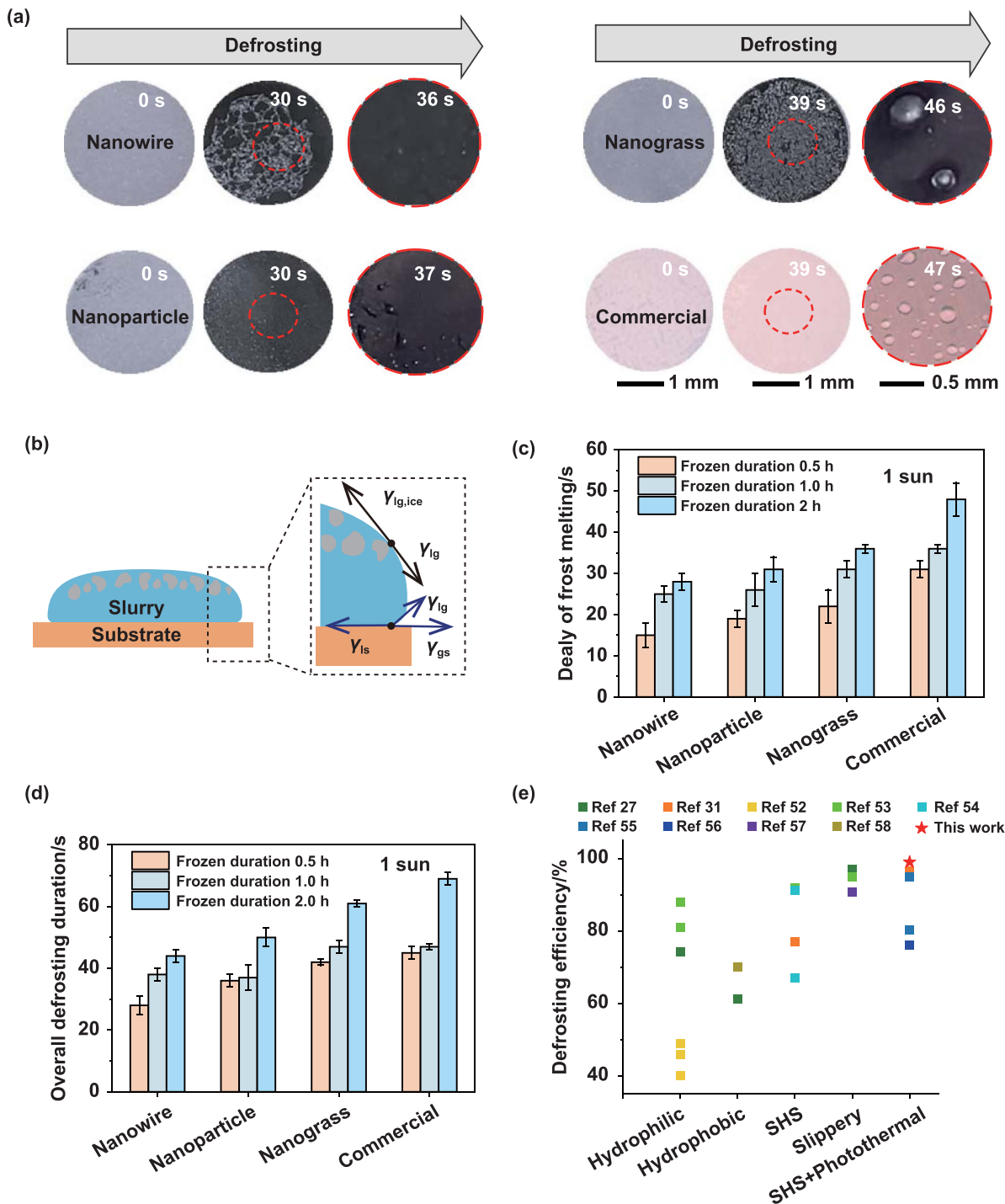
**Figure 6.** Photothermal defrosting performance. (a) Optical images showing the process of frost melting after being frozen for 1 h under one-sun illumination at $T_s = -10$ °C, $T_{air} = -10 \pm 1$ °C. (b) Schematic of forces acting on frost slurries during melting. (c) Delay of frost melting and (d) durations required to complete the defrosting process after the surfaces have been frozen for 0.5, 1, and 1.5 h under one-sun illumination. (e) Comparison of defrosting efficiency among our work and previous works [28, 32, 54–60], SHS is short for the superhydrophobic surface.

## 5. Conclusions

To summarize, we developed a facile template-assisted electrodeposition fabrication method to obtain highly ordered copper nanowire assemblies with controlled pattern, hierarchy, and size by simply adjusting the template dimensions and electrodeposition time. We found that nanowire assemblies with micro-groove patterns exhibited the superior ability to absorb sunlight (>95%). Facilitated by the good thermal conductivity of the surfaces, the absorbed heat can be effectively transported to the entire surface, thus showing a higher temperature rise than the other three nanostructured surfaces

upon receiving the sun illumination. This facilitated the melting of both localized frozen water and the global frost layer, especially on nanowire surface with upright nanowires and an average microgroove width of 2–3 $\mu$m. Further assisted by the superhydrophobic property, the nanowire assemblies manifested an advantage in spontaneous and prompt meltwater removal over other nanostructured surfaces with either superhydrophobicity, photothermal effect, or a combination of both properties. In particular, our design demonstrated the highest defrosting efficiency compared to previous studies. Infusing the easy fabrication, high controllability, and diversity in morphology, we expect that the design of nanowire assemblies can remove the need for energy input in broad de-icing and defrosting applications.

# 6. Experiments

## 6.1. Materials

Aluminum sheets and copper plates were purchased from Oudifu Technology, while high-purity aluminum sheets were supplied by Beijing Purui Advanced Material Technology Co., LTD The chemicals involving phosphoric acid, oxalic acid, perchloric acid, chromic acid, cupric pyrophosphate, potassium pyrophosphate, ammonium citrate tribasic, copper chloride, hydrochloric acid, sodium chlorite, trisodium phosphate dodecahydrate, and octadecanethiol, to name a few were obtained from Mucklin. Ethanol, acetone, and NaOH solutions were provided by Tianjin Kemiou Chemical Reagent Co., Ltd. Thermal grease was purchased from Pinsai Co., Ltd.

## 6.2. Methods

### 6.2.1. Fabrication of AAO    The AAO templates were prepared using the anodization method. First, aluminum sheets (99.999% purity, 0.4 mm thickness, diameter $\sim$80 mm) were annealed at 500 °C in the air for 2 h. Second, the oxide layer of the aluminum sheets was removed with 2 M NaOH solution, followed by the electropolishing treatment with HClO$_4$/ethanol solution at a volume ratio of 1:4 for 5 min at 21 V and 1 °C. Afterward, the resulting aluminum sheets were anodized in a rigorously stirred bath for 8 h at 1 °C, with the solution temperature controlled by a chiller (DFY-10L/25, Yuhua Co., Ltd). The electrolytes consisted of a 0.3 M oxalic acid solution mixed with 3 wt.% phosphoric acid in varying volume ratios. The second anodization was performed under the same conditions as the first anodization, where removing the disordered porous oxide film required the use of the solution of 30 g l$^{-1}$ CrO$_3$ and 50 ml l$^{-1}$ H$_3$PO$_4$. The back side of the aluminum sheets was then dissolved in a solution of 0.1 M CuCl$_2$ and HCl at a volume ratio of 9:1. Finally, the desired AAO templates were obtained after the barrier layer removal using a 5 wt.% H$_3$PO$_4$ solution.

### 6.2.2. Fabrication of nanowire assemblies.    All surfaces were fabricated by the electrodeposition assisted by an AAO

template. Before electrodeposition, the copper plates (thickness $\sim$2 mm, diameter $\sim$25 mm) were sequentially polished with 800, 2000, and 3000-grit sandpaper and ultrasonically cleaned with anhydrous toluene, ethanol, and deionized water successively, for 5 min to remove the oxidated layer and fouling. In brief, a copper disk, an anodic alumina oxide template, a filter paper infiltrated with an electrolyte solution, and another copper disk were laminated together. The electrolyte solution consisted of cupric pyrophosphate, potassium pyrophosphate, ammonium citrate tribasic, and deionized water at a weight ratio of 6:25:2:100 wt.%. The copper disk in contact with the template served as a cathode, while the other disk served as an anode. The lamination was then brought to electroplating at −0.8 V for 1200 s. Afterward, the cathode copper disk together with the template was transferred to the galvanizing bath and electro-plated at −0.8 V for 3 h. After the electrodeposition, the nanowire surfaces on the copper disk were obtained by etching the template in 2 M NaOH solution and were then washed with deionized water. All samples underwent a hydrophobic treatment by immersing in a 2.5 mM octadecanethiol ethanol solution at 70 °C for 1 h.

### 6.2.3. Fabrication of three nanostructured surfaces.    Nanoparticle surface was obtained by evenly moving it back and forth above the flame of a paraffin candle to deposit a carbon nanoparticle layer. Nanograss surface was fabricated by etching the copper plate in an alkaline solution consisting of NaClO$_2$, NaOH, Na$_3$PO$_4 \cdot$12H$_2$O, and deionized water at a weight ratio of 3.75:5:10:100 wt. % at 96 °C for 10 min. The surface was further immersed in a 2.5 mM octa-decanethiol ethanol solution at 70 °C for 1 h to be transformed into superrhydrophobic. Commercial surface was generated using the Neverwet product, which consisted of acetone, siloxane, and siloxane, via a simple spray method at a distance of 10 cm.

## 6.3. Characterization

### 6.3.1. Surface characterization.    The surface morphology was characterized by SEM (FEI Quanta 450 FEG, USA). The water contact angles and contact angle hysteresis of sample surfaces were measured using contact angle measurements (OCA 25, Dataphysics, Germany).

### 6.3.2. Photothermal measurement.    The spectral reflectivity and emissivity of the samples were measured by two different spectrophotometers (UH4150, Hitachi and VERTEX 70v, Bruker) following standard methods. To measure the surface temperature samples, both the infrared camera (HIKMICRO H13) and thermal couples (KPS-T-0.08-1000-CZ) were used. The samples were placed inside a jacketed beaker with a liquid (ethylene glycol water solution) circulating. By controlling the liquid temperature, the temperature of the ambient air inside the beaker could be maintained at a desired value, such as −10 °C. Three thermal couples with probe sizes of $\sim$80 $\mu$m were uniformly attached to the sample surfaces, and the temperature data was recorded by a temperature monitor (National

Instruments 9216). After the temperature of the entire system stabilized, the sample was illuminated with a sun simulator (CEL-HXF300-T10, Beijing China Education Au-light Technology Co., Ltd) that has a spectrum similar to solar radiation. The sun simulator was adjusted to be placed right atop the samples at a given distance, while the infrared camera was placed above the samples at a slight tilt angle.

*6.3.3. Deicing and defrosting experiment.* For the de-icing experiment, the samples were horizontally or obliquely attached to the thermally-insulated foam (TC160, Dataphysics) with thermal grease inside a jacketed beaker. The ambient air temperature inside the beaker could be maintained at $-15$ °C, $-20$ °C, and $-25$ °C by controlling the temperature of the circulating liquid. The relative humidity of the air was maintained at $20 \pm 3$%. After the experimental conditions reached stabilized, a droplet of 5 $\mu$l was gently released onto the sample surface and then got a quick freeze. The sun simulator was then turned on with the solar illumination of 1000 W m$^{-2}$. The de-icing process was monitored by a CCD camera (ZWSP-4KCH, Zhongwei Technologies CO., Ltd), as shown in figure S9. To image the condensed droplets and their relative positions with micro/nano structures underlying the frozen droplet, every sample was given a tilt angle of 90° to deliberately make the melted droplet slide off the surface. The substrate was then quickly placed onto a metallographic microscope (Eclipse LV100 ND, Nikon) to capture the condensed droplets located where originally placed the frozen droplet. For the defrosting experiment, the samples were first horizontally attached to a cooling device (TC160, Dataphysics) with thermal grease at $T_s = -20$ °C, RH = $50 \pm 3$%, $T_{air} = 15 \pm 1$ °C. After a frosting duration of 0.5, 1, and 1.5 h, the samples were quickly transferred to the beaker and horizontally placed on a foam. Afterward, the samples were exposed to the sun illumination with intensities of 500, 1000, and 1500 W m$^{-2}$. The de-frosting process was monitored by a CCD camera, as shown in figure S9.

## Acknowledgments

## Author contributions

X M conceived the research. S Y, Q L, and B D fabricated the samples. S Y and Q L carried out the deicing/defrosting experiments. Y Y, Y Z, and S G, Y J performed the reflectivity and emissivity experiments. S Y, Q L, B D, and R W conducted data and image analysis. Y J, X Q, and Y Y helped with the construction of experiment platform. S Y wrote the manuscript and all authors contributed to its final contents.

## Conflict of interest

The authors declare no competing financial interest.

## ORCID iD

Xuehu Ma ⓘ https://orcid.org/0000-0002-9496-3734

## References

[1] Mahvi A J, Boyina K, Musser A, Elbel S and Miljkovic N 2021 Superhydrophobic heat exchangers delay frost formation and enhance efficiency of electric vehicle heat pumps *Int. J. Heat Mass Transfer* **172** 121162

[2] Boyina K S, Mahvi A J, Chavan S, Park D, Kumar K, Lira M, Yu Y X, Gunay A A, Wang X F and Miljkovic N 2019 Condensation frosting on meter-scale superhydrophobic and superhydrophilic heat exchangers *Int. J. Heat Mass Transfer* **145** 118694

[3] Yang S Y, Wu C Y, Zhao G L, Sun J, Yao X, Ma X H and Wang Z K 2021 Condensation frosting and passive anti-frosting *Cell Rep. Phys. Sci.* **2** 100474

[4] Wang T, Zheng Y H, Raji A R O, Li Y L, Sikkema W K A and Tour J M 2016 Passive anti-icing and active deicing films *ACS Appl. Mater. Interfaces* **8** 14169–73

[5] Ramakrishna D M and Viraraghavan T 2005 Environmental impact of chemical deicers–a review *Water Air Soil Pollut.* **166** 49–63

[6] Parent O and Ilinca A 2011 Anti-icing and de-icing techniques for wind turbines: critical review *Cold Reg. Sci. Technol.* **65** 88–96

[7] Dhyani A, Choi W, Golovin K and Tuteja A 2022 Surface design strategies for mitigating ice and snow accretion *Matter* **5** 1423–54

[8] Xu Q, Li J, Tian J, Zhu J and Gao X F 2014 Energy-effective frost-free coatings based on superhydrophobic aligned nanocones *ACS Appl. Mater. Interfaces* **6** 8976–80

[9] Liu J, Zhu C Q, Liu K, Jiang Y L, Song Y, Francisco J S, Zeng X C and Wang J J 2017 Distinct ice patterns on solid surfaces with various wettabilities *Proc. Natl Acad. Sci. USA* **114** 11285–90

[10] Kim P, Wong T S, Alvarenga J, Kreder M J, Adorno-Martinez W E and Aizenberg J 2012 Liquid-infused nanostructured surfaces with extreme anti-ice and anti-frost performance *ACS Nano* **6** 6569–77

[11] Wong T S, Kang S H, Tang S K Y, Smythe E J, Hatton B D, Grinthal A and Aizenberg J 2011 Bioinspired self-repairing slippery surfaces with pressure-stable omniphobicity *Nature* **477** 443–7

[12] Leng X, Sun L C, Long Y J and Lu Y 2022 Bioinspired superwetting materials for water manipulation *Droplet* **1** 139–69

[13] Chatterjee R, Beysens D and Anand S 2019 Delaying ice and frost formation using phase-switching liquids *Adv. Mater.* **31** 1807812

[14] Irajizad P, Hasnain M, Farokhnia N, Sajadi S M and Ghasemi H 2016 Magnetic slippery extreme icephobic surfaces *Nat. Commun.* **7** 13395

[15] Azimi Dijvejin Z, Jain M C, Kozak R, Zarifi M H and Golovin K 2022 Smart low interfacial toughness coatings for on-demand de-icing without melting *Nat. Commun.* **13** 5119

[16] Golovin K, Dhyani A, Thouless M D and Tuteja A 2019 Low-interfacial toughness materials for effective large-scale deicing *Science* **364** 371–5

[17] Du B G, Cheng Y Q, Yang S Y, Xu W, Lan Z, Wen R F and Ma X H 2021 Preferential vapor nucleation on hierarchical tapered nanowire bunches *Langmuir* **37** 774–84

[18] Wen R F, Li Q, Wu J F, Wu G S, Wang W, Chen Y F, Ma X H, Zhao D L and Yang R G 2017 Hydrophobic copper nanowires for enhancing condensation heat transfer *Nano Energy* **33** 177–83

[19] Wen R F, Xu S S, Zhao D L, Lee Y C, Ma X H and Yang R G 2017 Hierarchical superhydrophobic surfaces with micropatterned nanowire arrays for high-efficiency jumping droplet condensation *ACS Appl. Mater. Interfaces* **9** 44911–21

[20] Wen R F, Ying Y S, Ma X H and Yang R G 2022 Sustainable anti-frosting surface for efficient thermal transport *Cell Rep. Phys. Sci.* **3** 100937

[21] Chu F Q, Wen D S and Wu X M 2018 Frost self-removal mechanism during defrosting on vertical superhydrophobic surfaces: peeling off or jumping off *Langmuir* **34** 14562–9

[22] Liang X C, Kumar V, Ahmadi F and Zhu Y Y 2022 Manipulation of droplets and bubbles for thermal applications *Droplet* **1** 80–91

[23] Yang S Y, Ying Y S, Li W B, Feng Y W, Wen R F, Li Q X, Liu Y B, Du B G, Wang Z K and Ma X H 2023 Efficient anti-frosting on discrete nanoclusters via spatiotemporal control of condensation frosting dynamics *Chem. Eng. J.* **465** 142991

[24] Lee W, Ji R, Gösele U and Nielsch K 2006 Fast fabrication of long-range ordered porous alumina membranes by hard anodization *Nat. Mater.* **5** 741–7

[25] Kaneko S, Urata C, Sato T, Hönes R and Hozumi A 2019 Smooth and transparent films showing paradoxical surface properties: the lower the static contact angle, the better the water sliding performance *Langmuir* **35** 6822–9

[26] Wang F, Liang C H, Yang M T, Fan C and Zhang X S 2015 Effects of surface characteristic on frosting and defrosting behaviors of fin-tube heat exchangers *Appl. Therm. Eng.* **75** 1126–32

[27] Shu C S, Su Q T, Li M H, Wang Z B, Yin S H and Huang S 2022 Fabrication of extreme wettability surface for controllable droplet manipulation over a wide temperature range *Int. J. Extrem. Manuf.* **4** 045103

[28] Yang S Y, Li W B, Song Y J, Ying Y S, Wen R F, Du B G, Jin Y K, Wang Z K and Ma X H 2021 Hydrophilic slippery surface promotes efficient defrosting *Langmuir* **37** 11931–8

[29] Gurumukhi Y *et al* 2020 Dynamic defrosting on superhydrophobic and biphilic surfaces *Matter* **3** 1178–95

[30] Mitridis E, Schutzius T M, Sicher A, Hail C U, Eghlidi H and Poulikakos D 2018 Metasurfaces leveraging solar energy for icephobicity *ACS Nano* **12** 7009–17

[31] Wu C Y, Geng H Y, Tan S C, Lv J Y, Wang H Q, He Z Y and Wang J J 2020 Highly efficient solar anti-icing/deicing via a hierarchical structured surface *Mater. Horiz.* **7** 2097–104

[32] Xie Z T, Wang H, Li M, Tian Y, Deng Q Y, Chen R, Zhu X and Liao Q 2022 Photothermal trap with multi-scale micro-nano hierarchical structure enhances light absorption and promote photothermal anti-icing/deicing *Chem. Eng. J.* **435** 135025

[33] Wu S W, Du Y J, Alsaid Y, Wu D, Hua M T, Yan Y C, Yao B W, Ma Y F, Zhu X Y and He X M 2020 Superhydrophobic photothermal icephobic surfaces based on candle soot *Proc. Natl Acad. Sci. USA* **117** 11240–6

[34] Zhang H Q *et al* 2021 Solar anti-icing surface with enhanced condensate self-removing at extreme environmental conditions *Proc. Natl Acad. Sci. USA* **118** e2100978118

[35] Yin X Y, Zhang Y, Wang D A, Liu Z L, Liu Y P, Pei X W, Yu B and Zhou F 2015 Integration of self-lubrication and near-infrared photothermogenesis for excellent anti-icing/deicing performance *Adv. Funct. Mater.* **25** 4237–45

[36] Dash S, De Ruiter J and Varanasi K K 2018 Photothermal trap utilizing solar illumination for ice mitigation *Sci. Adv.* **4** eaat0127

[37] Liu L, Xiong W, Lu Y, Huang X, Liu H, Fan L S, Jiang L, Silvain J F and Lu Y F 2019 Precise assembly and joining of silver nanowires in three dimensions for highly conductive composite structures *Int. J. Extrem. Manuf.* **1** 025001

[38] Li Y B, Zheng M J and Ma L 2007 High-speed growth and photoluminescence of porous anodic alumina films with controllable interpore distances over a large range *Appl. Phys. Lett.* **91** 073109

[39] Pokroy B, Kang S H, Mahadevan L and Aizenberg J 2009 Self-organization of a mesoscale bristle into ordered, hierarchical helical assemblies *Science* **323** 237–40

[40] Bico J, Roman B, Moulin L and Boudaoud A 2004 Elastocapillary coalescence in wet hair *Nature* **432** 690

[41] Eisner T and Aneshansley D J 2000 Defense by foot adhesion in a beetle (*Hemisphaerota cyanea*) *Proc. Natl Acad. Sci. USA* **97** 6568–73

[42] Betz O and Kölsch G 2004 The role of adhesion in prey capture and predator defence in arthropods *Arthropod Struct. Dev.* **33** 3–30

[43] Nicolson M 1949. The interaction between floating particles *Mathematical Proc. Cambridge Philosophical Society ed* B J Green (Cambridge University Press) pp 288–95

[44] Neukirch S and Van Der Heijden G H M 2002 Geometry and mechanics of uniform *n*-plies: from engineering ropes to biological filaments *J. Elast.* **69** 41–72

[45] Mandal J, Fu Y K, Overvig A C, Jia M X, Sun K R, Shi N N, Zhou H, Xiao X H, Yu N F and Yang Y 2018 Hierarchically porous polymer coatings for highly efficient passive daytime radiative cooling *Science* **362** 315–9

[46] Wang T, Wu Y, Shi L, Hu X H, Chen M and Wu L M 2021 A structural polymer for highly efficient all-day passive radiative cooling *Nat. Commun.* **12** 365

[47] Wang D H *et al* 2020 Design of robust superhydrophobic surfaces *Nature* **582** 55–59

[48] Quéré D 2008 Wetting and roughness *Annu. Rev. Mater. Res.* **38** 71–99

[49] Kwak K and Kim C 2005 Viscosity and thermal conductivity of copper oxide nanofluid dispersed in ethylene glycol *Korea Aust. Rheol. J.* **17** 35–40

[50] Enright R, Miljkovic N, Dou N, Nam Y and Wang E N 2013 Condensation on superhydrophobic copper oxide nanostructures *J. Heat Transfer* **135** 091304

[51] Jung S, Tiwari M K and Poulikakos D 2012 Frost halos from supercooled water droplets *Proc. Natl Acad. Sci. USA* **109** 16073–8

[52] Wen R F, Xu S S, Ma X H, Lee Y C and Yang R G 2018 Three-dimensional superhydrophobic nanowire networks for enhancing condensation heat transfer *Joule* **2** 269–79

[53] Boreyko J B, Srijanto B R, Nguyen T D, Vega C, Fuentes-Cabrera M and Collier C P 2013 Dynamic defrosting on nanostructured superhydrophobic surfaces *Langmuir* **29** 9516–24

[54] Wu X M, Chu F Q, Ma Q and Zhu B 2017 Frost formation and frost meltwater drainage characteristics on aluminum surfaces with grooved structures *Appl. Therm. Eng.* **118** 448–54

[55] Heu C S, Kim S W, Kim J, Lee S, Kim J M, Lee K S and Kim D R 2018 Frosting and defrosting behavior of slippery surfaces and utilization of mechanical vibration to enhance defrosting performance *Int. J. Heat Mass Transfer* **125** 858–65

[56] Shen Y Z, Jin M M, Wu X H, Tao J, Luo X Y, Chen H F, Lu Y and Xie Y H 2019 Understanding the frosting and defrosting mechanism on the superhydrophobic surfaces with hierarchical structures for enhancing anti-frosting performance *Appl. Therm. Eng.* **156** 111–8

[57] Wang B Q *et al* 2022 Ultraflexible photothermal superhydrophobic coating with multifunctional applications based on plasmonic tin nanoparticles *Adv. Opt. Mater.* **10** 2200168

[58] Zhang L, Gao C L, Zhong L S, Zhu L M, Chen H, Hou Y P and Zheng Y M 2022 Robust photothermal superhydrophobic coatings with dual-size micro/nano structure enhance anti-/de-icing and chemical resistance properties *Chem. Eng. J.* **446** 137461

[59] Zhou L P, Liu A W, Zhou L Z, Li Y R, Kang J, Tang J, Han Y N and Liu H T 2022 Facilely fabricated self-lubricated photothermal coating with long-term durability and external-replenishing property for anti-icing/deicing *ACS Appl. Mater. Interfaces* **14** 8537–48

[60] Schmiesing N C and Sommers A D 2017 Defrosting performance on hydrophilic, hydrophobic, and micro-patterned gradient heat transfer surfaces *Sci. Technol. Built Environ.* **23** 946–59